Geocoding and validation of ERS-1 InSAR-derived digital elevation models

David Small, Charles Werner, and Daniel Nüesch

Remote Sensing Laboratories
University of Zürich
Winterthurerstrasse 190
CH-8057 Zürich; Switzerland
Fax: +41 1 362 52 27; e-mail: daves@rsl.geogr.unizh.ch

ABSTRACT

Although the field of repeat-pass SAR interferometry (InSAR) has matured significantly in recent years, a comprehensive accuracy assessment of interferometrically-produced Digital Elevation Models (DEMs) has been lacking. Validation of the interferometric height model has been generally restricted to a few tens of tiepoints. Rigorous quality control requires large areal comparisons to a high-quality reference DEM. We present here results from the generation of geocoded ERS-1 InSAR DEMs for areas near Bern, Switzerland and Bonn, Germany. The accuracy of InSAR-derived DEMs is best evaluated in the map geometry of the reference DEM. As reference elevation models, we use the 25 metre resolution "DHM25" data set from the Swiss Federal Office of Topography, and a 1 arc second DEM provided by the German PAF. The preliminary InSAR processing steps are reviewed, the geocoding methodology is described, and the interferometrically derived heights are compared to the reference elevation model. Global RMS accuracies of 2.7 m were achieved over a 12 x 13 km area of moderate relief near the German city of Bonn.

1. INTRODUCTION

Although progress in the field of repeat-pass SAR Interferometry (InSAR) has been substantial in recent years, height accuracy estimates have been generally restricted to a few tens of control measurements (Zebker *et al.*, 1994). A recent report stated:

> *"Despite the widespread interest in interferometry with repeat orbits of ERS-1, surprisingly few quantitative assessments of complex data quality have been reported. This seems to apply both to the quality of the input low-level data products and also to the high-level derived products such as digital terrain maps."* (Hutchins, 1994).

Others have begun to deal with the validation of low-level products (Bamler and Just, 1993). This paper is aimed at the second question, the validation of ERS-1 repeat orbit InSAR-derived digital elevation models. An exhaustive literature search revealed one paper that had dealt with the related subject of the geocoding of two-antenna (single pass) airborne InSAR data (Madsen *et al.*, 1993). However the geolocation algorithm described there is not applicable to the ERS-1 repeat pass case, as the interferometric baseline is dynamic rather than static (within each patch). The ERS-1 repeat-pass case was treated in (Hartl and Thiel, 1993), but accuracies were only computed for highly-correlated corner reflectors, with graphical height comparisons otherwise limited to single transects (for which no achieved height accuracy figures were provided). Unidimensional height transects have also been compared using Seasat-InSAR (Lin *et al.*, 1992b), but RMS "accuracies" of only 110 m were attained. Indirect validation results were reported in (Massonnet *et al.*, 1993), where residual DEM fringes were used to confirm a reference DEM vertical accuracy of 24-30 m. However the poor accuracy of the reference DEM prevented validation of the interferometric heights themselves. Few height validation details were provided, as the concentration was understandably on differential InSAR results.

Here we provide an *areal* validation of repeat-pass satellite InSAR-derived height maps. Global RMS accuracies of 2.7 m are achieved over a 12 x 13 km area. Only minimal systematic biases in the height estimates are visible over an ERS-1 40 x 50 km quarter-scene.

Keywords: SAR Interferometry, Geocoding, ERS-1, DEM

2. METHOD

In this section, we briefly describe each of the InSAR processing stages. The two SLC products of interest are first registered precisely, followed by calculation of the interferogram, removal of orbital fringes through "flattening", calculation of the coherence, adaptive filtering, phase unwrapping, refinement of the geometry, and calculation of the interferometric height.

2.1 Registration

An automatic registration technique has been implemented, requiring no coarse offset estimates from an operator. The method operates at three levels:

1. Coarse range and azimuth offset estimates are calculated using the available orbit information (Small *et al.*, 1993a).

2. A large moving window around the orbital estimate is searched for the best FringeSNR (Gabriel and Goldstein, 1988) and a bounding box of possible offset values is calculated.

3. The bounding box is used to regulate calculation of approximately 250 (default setting) image chip locations distributed across range and azimuth.

The offset estimates with a fringe SNR above a set threshold are then input to a bilinear fit (with respect to range and azimuth) that models the registration. The absence of any required operator intervention allows multiple scene pairs to be calculated in batch mode. The importance of this capability was demonstrated when the software was installed at the German Processing and Archiving Facility (D-PAF).

More refined registration techniques may be necessary in mountainous regions to combat topography-induced registration errors (Lin *et al.*, 1992a). Parallax (the phenomenon used in Stereo-SAR) leads to different range positions for pixels at different elevations. Incorporation of an existing coarse elevation model during the registration process would mitigate this problem.

2.2 Interferogram Calculation

The bilinear offset functions shown above are used to define the location in SLC image 2 corresponding to each point in SLC image 1. Interpolation of SLC image 2 is performed blockwise in azimuth in the frequency domain by making use of the fact that the slope of the azimuth offset as a function of azimuth position is comparatively small, and that convolution with a delta function (i.e. offset) in the spatial domain is equivalent to multiplication with a pure phase term (exponential) in the frequency domain. Non-overlapping portions of the range spectra (Prati *et al.*, 1992) are masked out, significantly improving phase estimates for interferograms produced using large baselines. The present flat-terrain assumption within this step reduces the obtainable coherence in steep areas. Each range line is then oversampled and the second image is interpolated. Now that the two images have been co-registered, the N-look intensity-normalized complex interferogram $\hat{G}$ can be calculated:

$$G = \sum_{i}^{N} s_{1,i} s_{2,i}^{*} \; ; \qquad \hat{G} = \frac{\sum_{i}^{N} s_{1,i} s_{2,i}^{*}}{\sqrt{S_1 \cdot S_2}} \tag{1}$$

The N-look single-scene intensities S_1 and S_2,

$$S_1 = \sum_{i}^{N} s_{1,i} s_{1,i}^{*} \quad \textit{and} \quad S_2 = \sum_{i}^{N} s_{2,i} s_{2,i}^{*} \tag{2}$$

are calculated from the single look complex values s_1 and s_2, and stored for future reference. The interferogram is normalized by the two single-scene intensities to counteract the influence of bright point targets that might otherwise dominate the calculation of the FringeSNR. Such normalization is also discussed in (Massonnet *et al.*, 1993a). The normalized interferogram $\hat{G}$ then has magnitude equal to the N-look coherence. Although we switch from short integer IQ (SLC) to floating point storage (interferogram) at this stage, file size is nevertheless reduced, as N = 5 azimuth looks are taken.

2.3 Orbital "Flattening"

In preparation for the phase-unwrapping step to come, the range and azimuth phase trends ("orbital fringes") are removed, producing a "flattened" interferogram $\hat{F}$ that is much easier to unwrap. The baseline model is used to approximate the expected range phase term (Small *et al.*, 1993b),

$$\phi_i \approx \frac{4\pi}{\lambda} \cdot \frac{f_{1,i} \cdot B_j}{|f_{1,i}|} \tag{3}$$

where $f_{1,i}$ is the flat Earth look vector at range position i, and $\boldsymbol{B}_j$ is the baseline at azimuth position j. The range phase term is then removed temporarily from the complex interferogram $\widehat{\boldsymbol{G}}$ to produce the "flattened" interferogram $\widehat{\boldsymbol{F}}$:

$$\widehat{F}_i = \widehat{G}_i \cdot e^{-j\phi_i} \tag{4}$$

where $j = \sqrt{-1}$.

2.4 Coherence Calculation

For two N-look complex SAR images S_1 and S_2, we calculate the interferometric coherence γ as:

$$\gamma = \frac{\frac{1}{MN}\left|\sum_{k=1}^{M} \widehat{F}_k \cdot \sqrt{S_{1,k} \cdot S_{2,k}}\right|}{\sqrt{\frac{1}{MN}\sum_{k=1}^{M} S_{1,k}}\sqrt{\frac{1}{MN}\sum_{k=1}^{M} S_{2,k}}} \tag{5}$$

Using ERS-1 standard quarter scenes, we usually set N = 5 (all in azimuth), and M = 9 (3 each in range and azimuth). Note that (5) is equivalent to direct summation over an M x N window, since:

$$\sum_{i=1}^{MN} s_{1,i} s_{2,i}^{*} = \sum_{k=1}^{M}\left(\sum_{i=1}^{N} s_{1,i} s_{2,i}^{*}\right) = \sum_{k=1}^{M} G_k \tag{6}$$

and:

$$\sum_{i=1}^{MN} s_{1,i} s_{1,i}^{*} = \sum_{k=1}^{M}\left(\sum_{i=1}^{N} s_{1,i} s_{1,i}^{*}\right) = \sum_{k=1}^{M} S_{1,k} \tag{7}$$

The two step calculation results in a significant reduction in the computational cost of the coherence calculation. For the 15 x 3 case, the number of complex addition operations required per term is reduced by a factor of 3.2 (from 45 to 9 + 5 = 14). Given that the N-look interferogram and intensity files are already calculated (true in our case), the savings factor is increased to 5 (N in general).

Note that the coherence is calculated from the flattened interferogram $\widehat{\boldsymbol{F}}$, and not the original $\widehat{\boldsymbol{G}}$. This method is also used by (Massonnet *et al.*, 1993a). This is absolutely necessary when working with large baselines to avoid biasing from the range phase trend, which otherwise causes severe underestimation of γ. Given that one already has a high resolution elevation model, biases introduced to the coherence estimation by local slopes can be removed by calculating the phase difference expected due to the topography (Massonnet *et al.*, 1993b).

2.5 Adaptive Filtering

Phase unwrapping becomes very difficult in areas where phase estimates are ambiguous (e.g. forest). To reduce phase noise, a band-pass filter weighting function of width inversely proportional to the local coherence is applied to $\widehat{\boldsymbol{F}}$, producing a filtered interferogram $\widehat{\boldsymbol{F}}'$ Phase variation is reduced, while phase slopes are preserved (Small *et al.*, 1994). Adaptive smoothing allows the phase unwrapping step to proceed unencumbered by high phase noise.

2.6 Phase Unwrapping

The flattened unwrapped phase ϕ_{UF} was calculated from the filtered interferogram $\widehat{\boldsymbol{F}}'$ using an improved version of the classical residue-based method (Goldstein *et al.*, 1988). Areas that were unreachable by the algorithm were marked together with those of low coherence for future reference.

2.7 Refinement of Geometry

2.7.1 Imaging Geometry

The imaging geometry in the slant range direction is modelled as a linear function, with $|\boldsymbol{r}_{1,n}|$ the near range boundary, δ_r the slant range pixel spacing, and i the range pixel coordinate. The azimuth axis is a linear function of time, with t_0 the scene start-time, δ the N-look azimuth pixel spacing, and j the azimuth pixel coordinate. The values of $|\boldsymbol{r}_{1,n}|$, δ_r, t_0 and δ_t provided by the SAR processor are imprecise due to residual timing biases in the SAR (Li and Goldstein, 1990) as well as variation of the speed of light with ionospheric and atmospheric conditions (Roth *et al.*, 1993).

For the Swiss test scene tiepoints were measured from the Swiss 1:25000 map series, published by the Swiss Federal Office of Topography. In the German (Bonn) test scene, tiepoints were measured from topographic maps of the area produced by the German *Landesvermessungsamt Nordrhein-Westfalen* (1981).

Refinement of the imaging geometry requires positional tiepoints: the phase need not be locally homogenous, but

the range and azimuth positions must be accurately known. Bridges and road crossings are favoured candidates for such tiepoints, which are input to an iterative non-linear least squares estimation process (Marquadt, 1963) for refinement of $|\boldsymbol{r}_{1,n}|$, δ_r, t_0 and δ_t. The orbit itself may also be refined, although experience has shown (Roth *et al.*, 1993) that improvement of the near range boundary $|\boldsymbol{r}_{1,n}|$, slant range pixel spacing δ_r, azimuth start time t_0, and azimuth pixel spacing δ_t suffices.

2.7.2 Baseline Geometry

The baseline is modelled as having linearly-varying cross-track, and constant vertical (normal) components:

$$\boldsymbol{B}_j = B_n \cdot \hat{n} + (B_c + \alpha \cdot t_j) \cdot \hat{c}, \tag{8}$$

where $\hat{\boldsymbol{c}}$ and $\hat{\boldsymbol{n}}$ are unit basis vectors of the TCN geometry described in (Small *et al.*, 1993b), B_c and B_n are constant components of the baseline in those two dimensions, and α an azimuth convergence factor. The baseline is related to the measured phase by:

$$\Phi_i = \frac{4\pi}{\lambda}\left(\sqrt{|r_{1,i}|^2 + |B_j|^2 - (2r_{1,i} \cdot B_j)} - |r_{1,i}|\right) - \phi_c \tag{9}$$

where ϕ_c is a phase constant. The baseline calculated from the orbit vectors is too imprecise to allow accurate height calculations (Li and Golstein, 1990), so an iterative non-linear least squares refinement (Levenberg-Marquadt) (Marquadt, 1963) of the baseline geometry is applied (Small *et al.*, 1993b). The baseline model is described by a "state vector" made up of four parameters: ϕ_c, B_c, α, B_n. Height tiepoints are ideally chosen in relatively flat areas of locally homogenous phase.

2.8 Height Calculation

The phase of the original interferogram ϕ_{UG} (now unwrapped) is first reconstructed from the unwrapped flattened phase ϕ_{UF} via:

$$\phi_{UG} = \phi_{UF} + \phi_i \tag{10}$$

This is simply the reversal of equation (4), which was applied to assist the phase unwrapping process. The difference in slant range distances between the two images is then calculated as:

$$\delta_i = \frac{\lambda}{4\pi} \cdot (\phi_{UG} + \phi_c) \tag{11}$$

where ϕ_c is a constant phase offset recovered from the refinement of the geometry (Small *et al.*, 1993b). All sides of the triangle formed by $\boldsymbol{r}_1$, $\boldsymbol{r}_2$ and $\boldsymbol{B}$ are now accurately known, enabling calculation of the internal angles using cosine law. This makes possible calculation of the c' and n' components $\boldsymbol{r}_{1,c',i}$ and $\boldsymbol{r}_{1,n',i}$ of the look vector. From figure 1 one sees that ground range difference $g_{d,i}$ may be calculated as:

$$g_{d,i} = g_i - g_c = \frac{r_{1,i}}{\sin(\theta_i + \beta)} - \left(\sqrt{r_{1,c}^2 - h^2}\right) \tag{12}$$

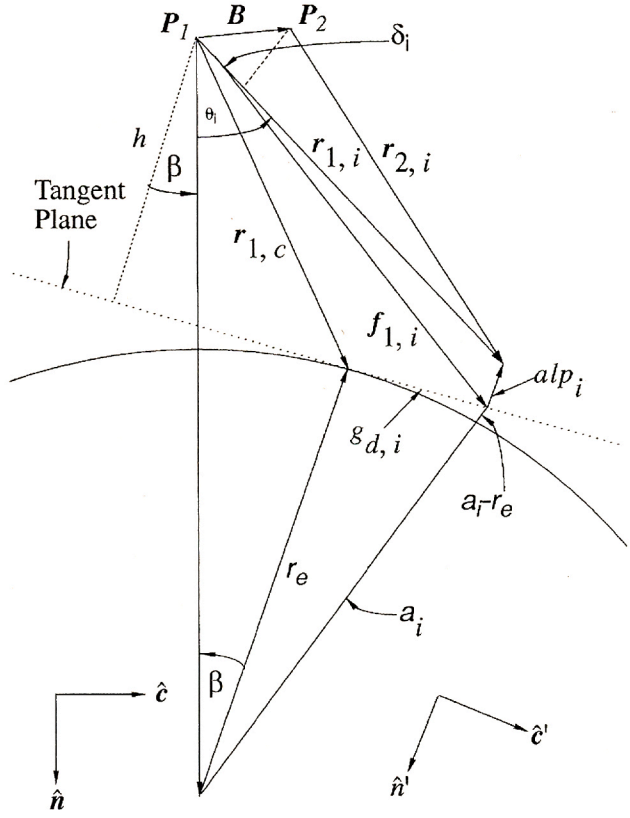

Figure 1 - InSAR tangent plane geometry.

where θ_i is the local incidence angle. The height above the tangent plane alp_i may be calculated via:

$$alp_i = h - r_{1,n',i'} \tag{13}$$

and the interferometrically derived height H_i may be estimated as:

$$H_i \cong alp_i + \left[\sqrt{r_e^2 + g_{d,i}^2} - r_e\right] \tag{14}$$

A height is computed for every point in the scene with the exception of those marked during the coherence calculation and phase unwrapping steps as lacking reliable phase

information (invalid). The heights of such pixels are calculated by interpolation over the local neighbourhood.

3. DEM VALIDATION

3.1 Terrain Geocoding

Hilly terrain can cause severe geometric distortions in SAR images. Layover and foreshortening distortions must be removed if one desires an accurate resampling of the SAR image into a map projection. Range-Doppler SAR geocoding algorithms have existed for some time (Curlander, 1982). Terrain geocoding software written at our institute has been installed at the D-PAF and used operationally since early 1992 to produce standard ERS-1 Geocoded-Terrain-Corrected "GTC" products (Schreier, 1993).

We have written a terrain geocoder capable of processing many of the InSAR data products described above. These include InSAR-produced elevation models, coherence maps, as well as conventional detected SAR images. An example of a conventional terrain-geocoded (Meier *et al.*, 1993) detected SAR image ("GTC") is seen in figure 2.

Terrain geocoding of such products has many applications:

- Validation of InSAR-derived height maps
- Investigation of class-dependent coherences (Small *et al.*, 1994)

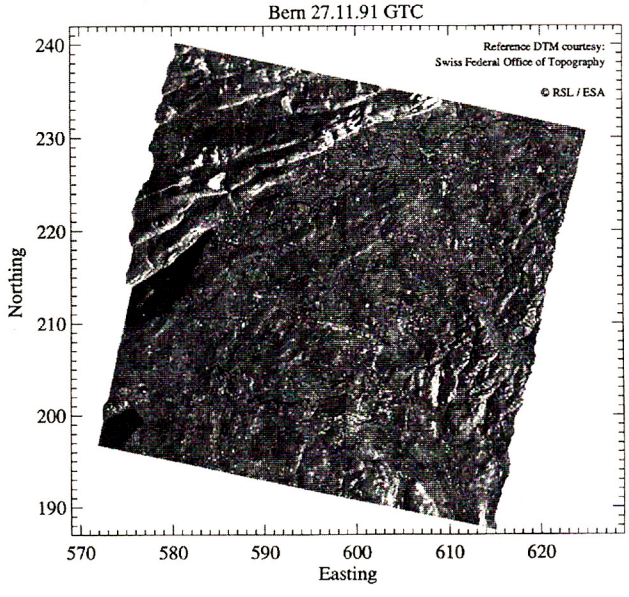

Figure 2 - Geocoded Terrain Corrected "GTC" detected ERS-1 SAR image (Bern 27.11.91).

- Investigation of ascending vs. descending coherences (Small *et al.*, 1994)
- Normalization for radiometric effects of topography (Holecz *et al.*, 1994)
- Differential Interferometry (Massonnet *et al.*, 1993)

This paper focuses on the validation of InSAR-derived height maps. Here we define height maps as heights referenced to a map projection system (i.e. *not* in slant range).

3.1.1 Coordinate Transformations

Geocoding naturally requires the ability to transform between global Cartesian coordinates (based for example on the WGS84 standard), and the map projection of interest (Frei *et al.*, 1993). The position of each point in the DEM is in turn transformed from the map projection in which it is stored as $\boldsymbol{P}\,(X_m, Y_m, H)$ into geographic coordinates as $\boldsymbol{P}\,(\lambda, \varphi, h)$. From there follow transformations into Cartesian coordinates based on a local datum, as $\boldsymbol{P}\,(X', Y', Z')$, and then Cartesian coordinates based on a global datum (e.g. WGS84), as $\boldsymbol{P}\,(X, Y, Z)$. In summary:

$$\boldsymbol{P}\,(X, Y, Z) = M\,\{L\,\{G\,\{P\,(X_m, Y_m, h)\}\ \}\ \} \qquad (15)$$

where $G\,\{\ \}$ is a transformation from the map coordinate system to geographic coordinates (latitude and longitude), $L\,\{\ \}$ is a transformation from geographic coordinates to local-datum-based Cartesian coordinates, and $M\,\{\ \}$ is a transformation from the local to global datum. Once the DEM positions are known in the global datum, they can be directly compared with the satellite orbit information, and used to refine the geometry, as described in Section 2.7.

3.1.2 Doppler Iteration

Since the DEM positions and satellite orbit are both known precisely, the Doppler frequency may be calculated as:

$$f_D = \frac{2}{\lambda}\left(\frac{P-S}{|P-S|}\cdot v\right) \qquad (16)$$

where $\boldsymbol{P-S}$ is the look vector from the satellite orbit to the DEM position, with S the satellite position, and v the instantaneous satellite velocity relative to the DEM position $\boldsymbol{P}$. The position j along the satellite track is iterated until the Doppler condition is satisfied (i.e. $f_D = f_{ref}$). A value of f_D above f_{ref} indicates that one should move forward in the orbit; a value below that of f_{ref} indicates that the cor-

rect orbit position lies behind the present value (Meier *et al.*, 1993).

3.1.3 Resampling

Once the Doppler condition is satisfied, the slant range position i is calculated as:

$$i = \frac{|P-S| - |r_{1,n}|}{\delta_r} \quad (17)$$

where $r_{1,n}$ is the slant range at the near-range edge, and δ_r is the slant range pixel spacing. Identification of both the azimuth position j and the slant range position i provides a precise reference within the slant range image. This has been an *object-to-image* transformation. Beginning in map coordinates M, we have established a connection to the slant range geometry S:

$$M(X_m, Y_m) \Rightarrow S(j, i). \quad (18)$$

Slant range values $S(\ )$, be they backscatter intensity, coherence, or interferometric height, can then be sampled into the DEM's map geometry using ones preferred interpolation method.

3.2 Geocoding without a reference DEM

Once both the baseline and imaging geometry have been refined (as described in section 2.7) terrain geocoding of the scene is possible without the *a priori* existence of a reference DEM. This is performed by calculating the look vector $\boldsymbol{L}$ corresponding to each range azimuth pixel and adding it to the orbital position $\boldsymbol{S}$:

$$\boldsymbol{P} = \boldsymbol{S} + \boldsymbol{L}. \quad (19)$$

This is an *image-to-object* transformation. Beginning in slant range, we establish a connection to the global datum (WGS84) and then map coordinates:

$$S(j, i) \Rightarrow M(X_m, Y_m). \quad (20)$$

This produces an irregularly gridded set of points $\boldsymbol{P}$ on the Earth's surface, which can be converted to a regular grid via (for example) Delauney Triangulation. Such triangulation is unfortunately very memory intensive: nearest neighbour interpolation requires less memory, but is less accurate.

4. RESULTS

We used two test sites for our quality assessment of InSAR-derived DEMs: one centred on the area between the cities of Bern and Solothurn in Switzerland, and another west of the city of Bonn in Germany. Shaded relief models of the reference DEMs are shown in figures 3 and 4.

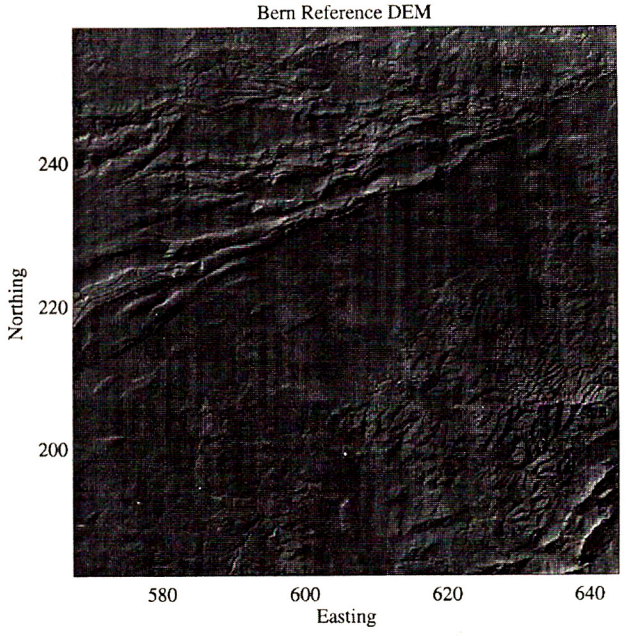

Figure 3 - Swiss reference DEM ("DHM25") as shaded relief, Courtesy of Swiss Federal Office of Topography.

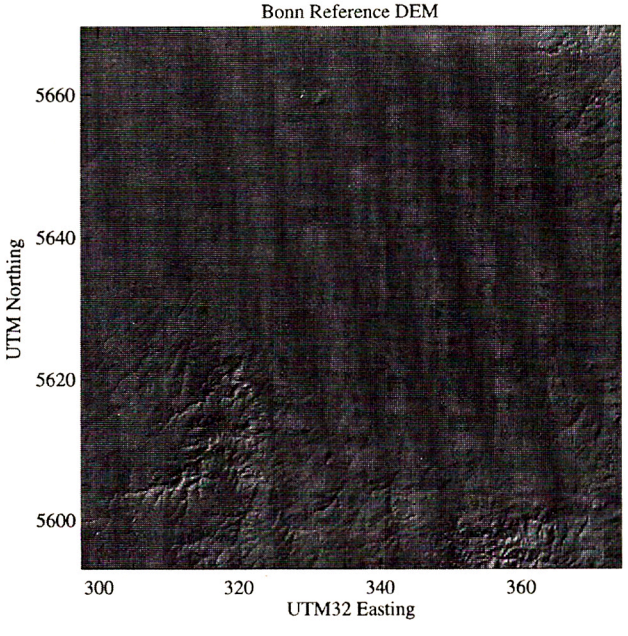

Figure 4 - German reference DEM as shaded relief (Courtesy of D-PAF).

The reference elevation model for the Bern area (see figure 3) was provided by the Swiss National Office of Topography. It is a high quality model derived from digitized map sheets, arranged in the Swiss national (oblique Mercator) map projection at an original horizontal grid spacing of 25 m. The heights are quantized to integer decimetres. Mean standard deviation of raster heights (compared with model measurements) is advertised as 2.66 m over the test area (Swiss Federal Office of Topography, 1993). The reference height model covers the entire SLC quarter scene.

The reference elevation model for the Bonn area was provided by the D-PAF (see figure 4). It was derived from digitized map sheets in the early 1980's, and has an original grid spacing of 1 arc second, but has been resampled into a 12.5 m horizontal grid spacing in the Universal Transverse Mercator (UTM) map system (zone 32). The heights are quantized to integer metres. The reference DEM covers the area of the entire SLC quarter scene.

Parameters relevant to our test scenes are summarized in Table 1. The acquisition dates are listed, as are the length of the baseline B_T, the component of the baseline perpendicular to the line-of-sight (slant range) direction $B_\perp$, and the component of the baseline parallel to the line-of-sight direction $B_\parallel$.

Table 1 - Scene information

	Dates	B_T [m]	$B_\perp$ [m]	$B_\parallel$ [m]	Node
Bern	27 / 24.11.91	69	-58	-37	Desc
Bonn	14 / 17.03.92	456	-420	-177	Desc
Bonn	14 / 20.03.92	984	-927	-329	Desc
Bonn	14 / 29.03.92	166	131	102	Desc

Note the lengths of the baselines between the Bonn 14.03.92 / 17.03.92 and 14.03.92 / 20.03.92 pairs. The critical baseline for ERS-1 is approximately 1300 m (Zebker *et al.*, 1992). The baseline between the 14.03.92 and 20.03.92 pair is close to the highest useful for interferometry, as at distances above the critical baseline, the range spectra no longer overlap, and all coherence is lost. Long before then, the range resolution has been reduced to suboptimal levels. The critical baseline B_{Cr} is calculated (Zebker *et al.*, 1992) as:

$$B_{Cr} = \frac{\lambda \rho}{2\delta_r} \cdot \tan\theta \qquad (21)$$

where λ is the radar wavelength, ρ the slant-range distance, δ_r the slant range resolution, and θ the incidence angle.

4.1 Bern, Switzerland

Terrain geocoding (as described in Section 3.1) allows resampling of any slant-range information into an arbitrary map projection. The slant range information can be either a detected SAR image (as in the standard ESA GTC product), the interferometric coherence (as described in Section 2.4), or the interferometric height (see Section 2.8).

Figure 5 shows the height model calculated from the Bern pair after terrain geocoding (as described in Section 3.1). As assistance in orientation (also in connection with figure 2), we note that the city of Bern is situated at (600,200), Lake Murten at (575,197), Lake Biel at (578,212), and the city of Solothurn at (608,228).

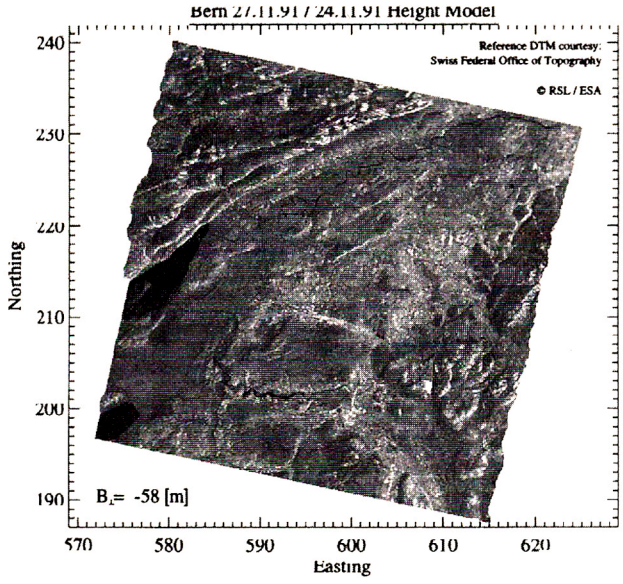

Figure 5 - Bern InSAR height map (colour cycle of length 300 m, intensity from SAR image).

See plate I at end of volume

Figure 6 shows the differences between the interferometrically measured height and that of the reference DEM.

One sees that the height accuracies are unacceptable in the Jura mountains in the northwest, as well as the southwest region close to Lake Murten. Phase unwrapping errors in the southeast are also apparent. In areas of low coherence (typically forest or water), phase variance is substantial, and height estimates are error-prone.

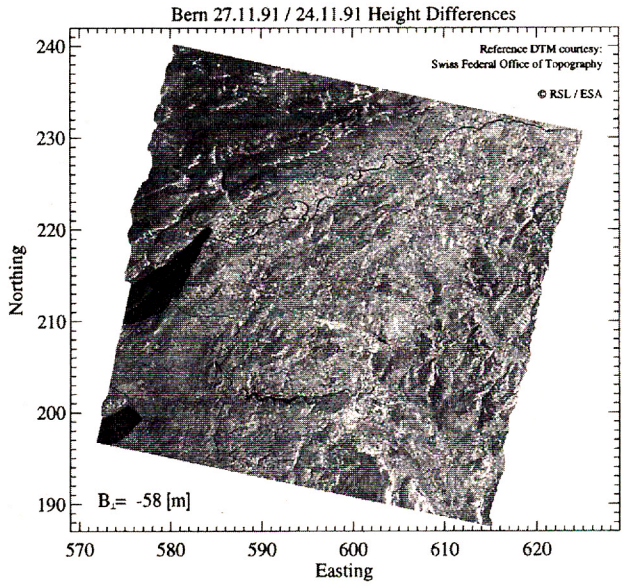

Figure 6 - Bern InSAR height differences, colour saturation scale -80 m (blue) to +80 m (red), intensity from SAR image.

See plate I at end of volume

Curiously, parts of Lake Murten produced unexpectedly high coherences (0.3-0.4). After some initial excitement, we relegated the phenomenon to correlated azimuth ambiguities, as neighbouring field boundary patterns were visible in the lake's coherence image. Lake Biel, in contrast, conformed to expectation, exhibiting the familiar low coherences of open water. Within Lake Biel the nearest high coherence shoreline height estimates were used as endpoints for interpolation. The shore height estimates are themselves however not reliable (particularly on the NW shore), due to the severe slopes in the area. The large height differences in the area surrounding Lake Murten could be due to systematic error sources, although the good results seen in figure 10 and discussed in Section 4.2 speak against this hypothesis.

As described in Section 3.2, one can also create a geocoded DEM without the *a priori* existence of a reference elevation model. Because of the memory sensitivity of the triangulation, we only processed a small subscene along the Aare river. Areas marked as unreliable during the adaptive filter and phase unwrapping processing stages do not contribute points to the triangulation. Once the geocoded InSAR DEM has been triangulated, the reference DEM is subtracted for validation purposes. Figure 7 shows the distribution of the height differences. One sees that the interferometric height estimates are relatively unreliable in hilly forested areas, and along the river itself. A histogram of the height differences is shown in figure 8; a global RMS height accuracy of 23 m was measured over the area. The low accuracy achieved is largely due to the small baseline.

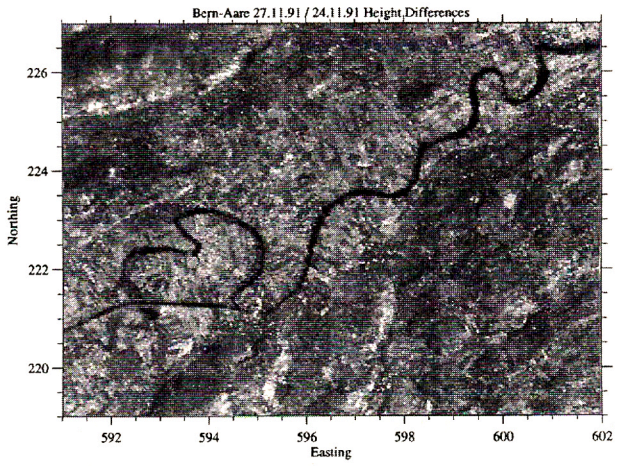

Figure 7 - Height difference map (Bern-Aare triangulated) Colour saturation scale from -40 m (blue) to +40 m (red), intensity from SAR image.

See plate I at end of volume

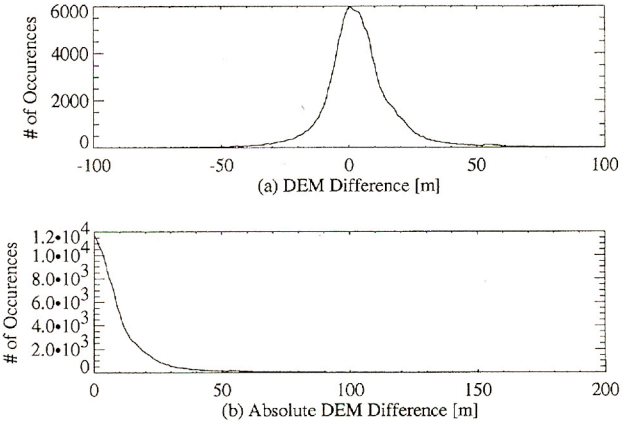

Figure 8 - Bern-Aare: (a) Histogram of height differences, (b) Histogram of absolute height differences.

4.2 Bonn, Germany

The terrain-geocoding process was also applied to data from an area west of the German city of Bonn. The geocoded interferometric height map is shown in figure 9. The difference between the InSAR-derived height and that of the reference model is shown in figure 10 (InSAR height - reference height). For orientation purposes, a coherence map of the area is shown in figure 11. The city of Bonn is located at approximately (365, 5620), Cologne (Köln) at (355, 5642), the Bonn-Cologne airport at (370, 5637), and the village of Nörvenich at (333, 5632). A large active open-pit brown coal (lignite) mine is located at (341, 5640).

Depending on the degree of trust that one is willing to assign the reference and InSAR-derived DEMs, figure 10

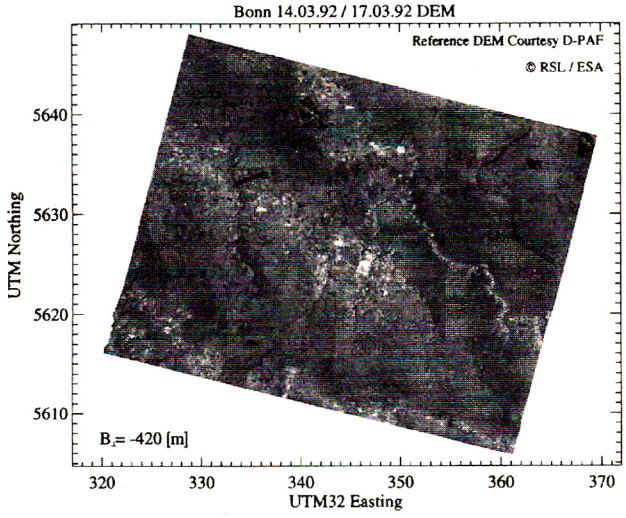

Figure 9 - InSAR height model (Bonn 14 / 17.03.92) Colour cycle of length 100 m, intensity from SAR image.

See plate I at end of volume

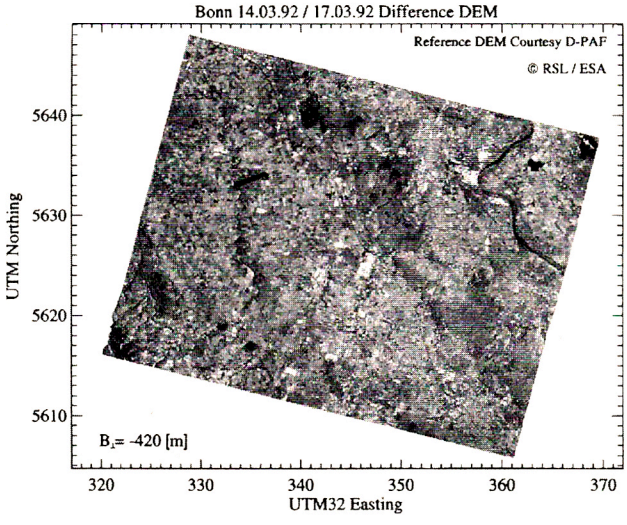

Figure 10 - Height difference map (Bonn 14 / 17.03.92) Colour saturation scale from -40 m (blue) to +40 m (red).

See plate I at end of volume

can be used to either validate the InSAR-derived height map, or highlight areas where the reference DEM requires updating.

The height differences shown indicate that in comparison to the Bern results shown previously, substantially better height accuracies are achieved in the Bonn scene. The improvement is due in large part to the longer baseline, which increases the height sensitivity. The largest height difference seen in figure 10 is due to the reference DEM not being up-to-date, and not an error in the InSAR height estimate. Many open-pit lignite mines are found in the region, and the reference DEM has not been updated to reflect mining activity. Areas of probable deposition can also be identified: material has most likely been removed from the open-pit mines and deposited as tailings elsewhere (see Section 4.2.3).

These areas excepted, the InSAR DEM is remarkably consistent with the reference. Differences are confined to a range of ±40 m, usually ±10 m, except where the phase unwrapping was unable to propagate into dense forest. The height differences in the SW corner of figure 10 are due to the phase unwrapping algorithm not being able to propagate into that hilly forested area. In the central eastern part of the scene, areas of forested hilly terrain produce larger height errors. A coherent phase anomaly (Wegmüller *et al.*, 1994) also shows itself in the area (335-342, 5623).

Figure 11 shows the coherence map calculated for the Bonn 14.03.92 / 17.03.92 pair. Coherence is scaled from 0 (black) to 1 (white). Agricultural fields show characteristically high coherences, while forests and rivers produce much lower ones. Towns and villages are relatively easily separable in this pair, exhibiting a mid-range coherence value (Wegmüller *et al.*, 1994). Examination of figure 11 gives one an idea of the degree to which one can generalize from analysis of the Bonn sub-scenes discussed below.

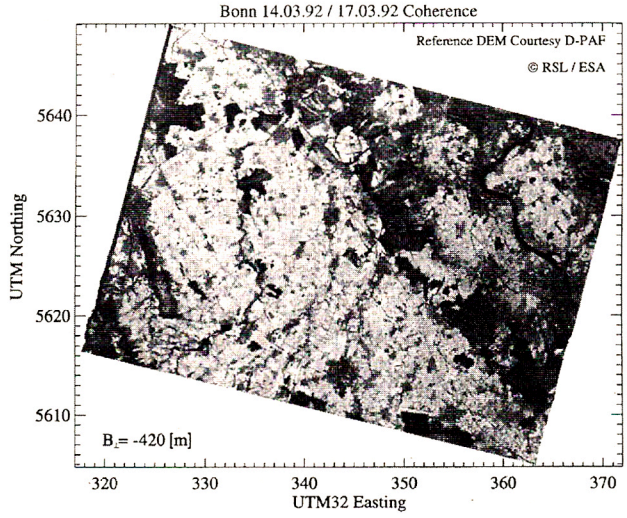

Figure 11 - ERS-1 coherence map (Bonn 14.03.92 / 17.03.92) Greyscale from 0 (black) to 1 (white).

4.2.1 Visualization

Figure 12 shows a 3D visualization of the Bonn-Cologne area landscape. The perspective view was calculated from the geocoded InSAR-derived height map with a program developed at RSL (Graf *et al.*, 1994). The elevation model is viewed from the north-east, at an altitude of 25 km: the Bonn-Cologne airport is visible in the foreground. The height map covers the same area seen in figure 9.

Figure 12 - Visualization of Bonn 14 / 17.03.92 InSAR DEM, viewed from NE: Heights depicted as colour cycle of length 100 m, intensity from SAR image.

See plate II at end of volume

4.2.2 Nörvenich Region

To reduce the size of the dataset a subscene was chosen as a DEM validation test site. The Nörvenich region within the Bonn scene is characterized by moderate topography, with a terrain variation of 80 metres, and relatively high coherences (though there are forested areas present with lower coherence values). Figure 13 shows the InSAR-derived height model of the area. The *Neffelbach* creek runs south to north through the centre of the area.

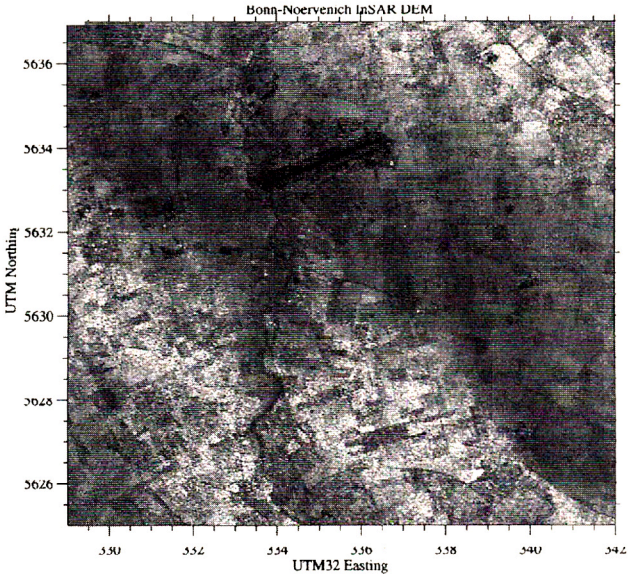

Figure 13 - InSAR height map (Bonn-Nörvenich 14 / 17.03.92) Colour cycle of length 50 m, intensity from SAR image.

See plate II at end of volume

The differences between the InSAR-derived height and that of the reference DEM are displayed in figure 14. Note the contour-like shapes. The interferometrically-derived heights at times clearly improve upon the reference DEM: the "holes" visible at (340.5, 5636.5), (340, 5631), and (333, 5635) are gravel pits not considered in the reference model. Otherwise, the InSAR-derived heights are in remarkably good agreement with the reference DEM.

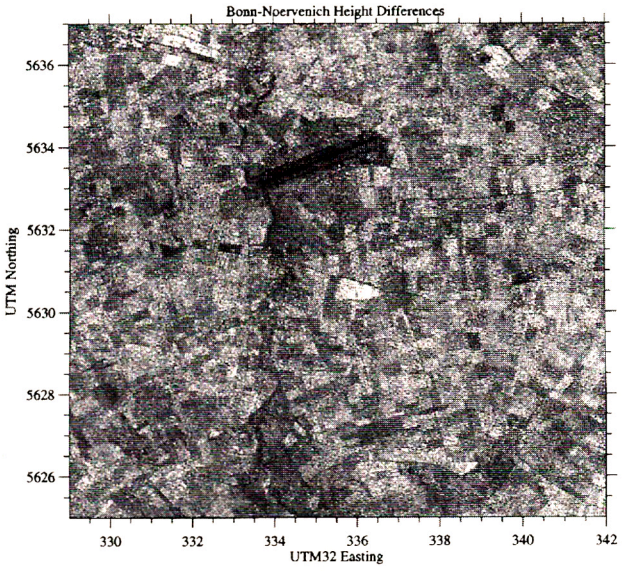

Figure 14 - Height difference map (Bonn-Nörvenich 14 / 17.03.92) Colour saturation scale from -20 m (blue) to +20 m (red).

See plate II at end of volume

Since height accuracy is expected to be dependent on the local coherence value, a coherence map is of interest for quality control purposes. Figure 15 shows a coherence map of the Nörvenich region. Comparison with figure 11 shows that the area has slightly higher coherence than is typical for the rest of the quarter-scene. Although most of the area is characterized by high coherence values, forested areas surrounding the airport and along the creek exhibit lower values. Visual comparison of figure 14 with figure 15 suggests a correlation between low coherence and larger height differences.

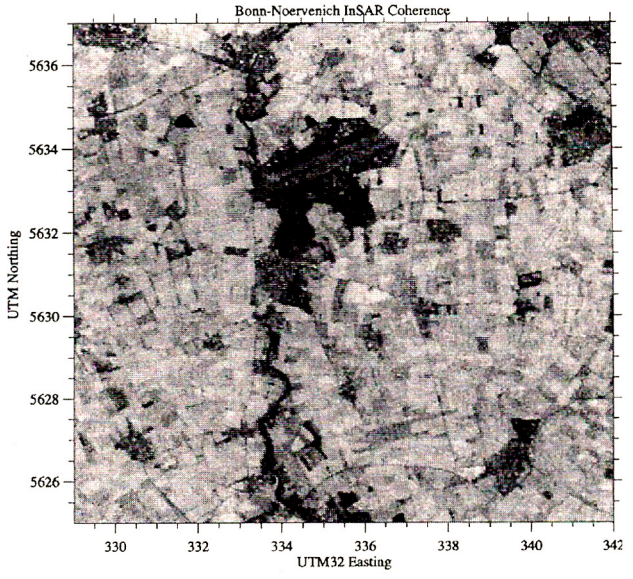

Figure 15 - Coherence map (Bonn-Nörvenich 14.03.92 / 17.03.92) Greyscale from 0 (black) to 1 (white).

Figure 16 shows the two-dimensional histogram of the height difference vs. the local coherence. Note the small height variation in the high-coherence areas, and that height differences increase with lower coherence. The RMS height difference was calculated to be 4.9 m for $\gamma < 0.2$ and 2.3 m for $\gamma > 0.8$. The mean coherence of the area was 0.82. Note that these measures underestimate the effect of low coherence, as the adaptive filter can cause neighbouring high coherence areas to dominate the local phase estimation.

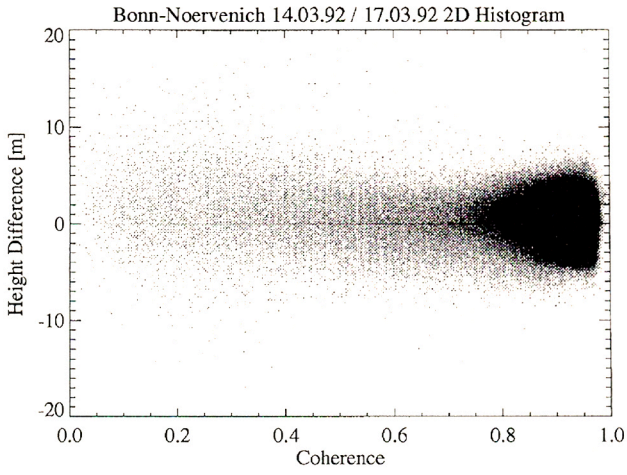

Figure 16 - Two dimensional histogram of height difference vs. coherence (Bonn-Nörvenich) 14.03.92 / 17.03.92.

Figure 17(a) displays a histogram of the differences between the InSAR-derived height and that of the reference DEM, at a one metre bin size. Figure 17(b) shows a histogram of the absolute height differences. Note that no significant systematic height bias is visible. The negligible bias that is present can be attributed to a difference in reference ellipsoids. The map heights (in the German

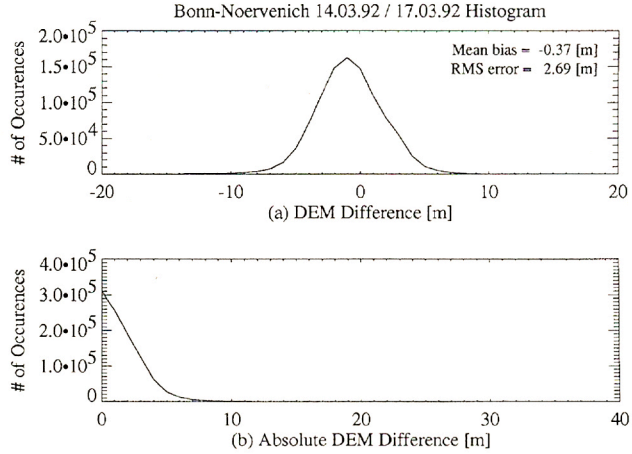

Figure 17 - Bonn-Nörvenich 14.03.92 / 17.03.92: (a) Histogram of height differences, (b) Histogram of absolute height differences.

Gauss-Krüger projection and associated datum shift), used during refinement of the geometry, differ from the reference heights in the DEM's UTM-associated datum shift. A global ellipsoidal shift is applied across the image to account for this; however, a small bias can remain.

A global RMS error of 2.7 m was achieved over the 12 x 13 km area. Considering the fact that the reference DEM is quantized to 1 m intervals, this is encouraging for the future of ERS-1 derived digital elevation model extraction. Note that the "error" figure is calculated over *all* pixels in the area.

We note that the smoothly undulating Bonn scene benefits from the spectral-shift filtering more than a relatively mountainous scene (e.g. Bern, even if one were to assume comparable baselines). Advanced InSAR processors might use a coarse elevation model to tailor the spectral filter to the local slope.

Height accuracy could be further improved by combination of ascending and descending passes over the same area (N.B. long baseline), by using the height value associated with the highest local ground resolution (Haefner *et al.*, 1993).

4.2.3 Open-Pit Coal Mining Region

There is intensive open-pit coal mining activity in the area southwest of the city of Cologne. The topographic maps identify mining areas as well as lakes that have formed in areas of former mining activity.

Figure 18 shows the difference between the InSAR-derived height and that of the reference DEM for the coal-mining region. Height differences saturate at limits of ±40 m. The reference DEM is seen to be out-of-date in some areas, as the interferometric height differs significantly. Excavation has occurred in many of the pits since the reference DEM was produced, while in other locations tailings have been deposited. This demonstrates the potential use of repeat-pass InSAR for updating digital elevation models.

4.2.4 Baseline Dependencies

Two other Bonn scene pairs were examined in addition to the 14.03.92 and 17.03.92 data already discussed (see Table 1). Although one would expect increased height sensitivity from the pair 14.03.92 / 20.03.92, due to its

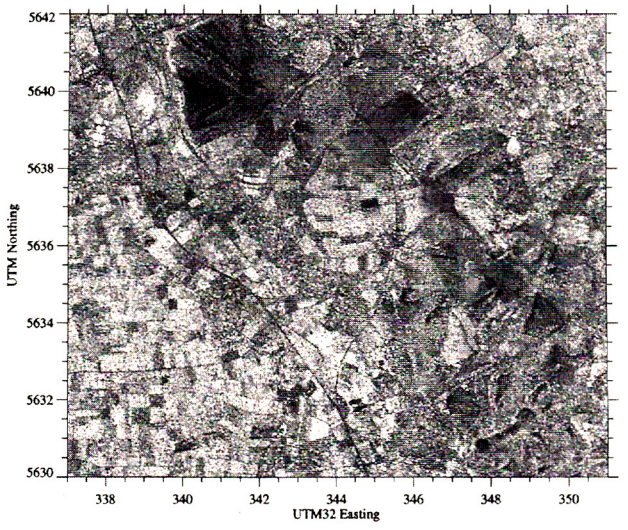

Figure 18 - Height difference map (Coal Mining Area 14 / 17.03.92) Colour saturation scale from -40 m (blue) to +40 (red).

See plate II at end of volume

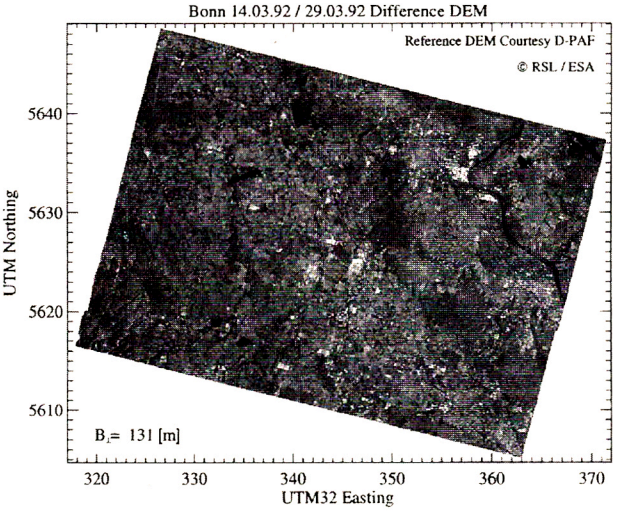

Figure 19 - Height difference map (Bonn 14 / 29.03.92) Colour saturation scale from -80 m (blue) to +80 m (red).

See plate II at end of volume

much larger baseline ($\boldsymbol{B}_\perp$ = -920 m), the high phase sensitivity makes phase unwrapping more difficult, and atmospheric propagation effects (Massonnet *et al.*, 1993b) become increasingly serious with larger baselines. The InSAR-derived height map is less consistent with the reference DEM than that achieved with the 14/17 pair.

The 14.03.92 / 29.03.92 pair has a smaller baseline, as well as a longer temporal interval. These two factors work to decrease the height sensitivity in comparison to the 14.03.92 / 17.03.92 pair. Previous work with the 14/29 pair was reported in (Small *et al.*, 1993b) and (Small *et al.*, 1993a), where height accuracies were determined using a set of tiepoints. Geocoded height comparisons allow a more systematic validation. Geocoding the height model and comparison with the reference DEM reveal the height differences seen in figure 19.

One sees that the less sensitive shorter baseline together with the extended period of decorrelation (15 days) create conditions less suitable for height extraction. In addition to what could be an elevation-dependent error influence in the southwest corner, local coherent phase anomalies are also visible at (335-342, 5624), and south of the airport (365, 5632). These could be due to local atmospheric phenomena (Wegmüller *et al.*, 1994) similar to those reported in (Massonnet *et al.*, 1994), although we have no meteorological evidence to support this speculation.

Within the Nörvenich region, the pair produces the height difference distribution seen in figure 20, with an RMS of 11.6 m, significantly worse than those obtainable with the longer baseline (and shorter repeat time interval) that are shown in figures 14 and 17. The RMS value is slightly higher, but on the same order as that previously reported in (Small *et al.*, 1993b). The long tail of the distribution seen in figure 20 is indicative of either large scale, perhaps propagation-change-dependent, coherent phase shifts, or (possibly) a systematic error source (tilt) in the processing. A comparison of figure 17 with figure 20 underscores the importance of large baselines and short time intervals for accurate height extraction using satellite repeat-pass interferometry.

4.3 Sources of Height Errors

Interferometric height measurements are subject to error influences (Li and Goldstein, 1990) originating in (a) imprecise knowledge of the slant range, baseline components, and absolute height, as well as (b) phase noise. The influence of phase noise decreases with increasing baseline distances. To test the success of our geometry refinement (see Section 2.7) in eliminating errors caused by imprecise knowledge of the geometry, we compared the residual RMS height error calculated for three different baseline distances. RMS height difference values were obtained for subscenes within three scene pairs. In the Bern-Aare region, RMS height differences of 23 m were obtained for a baseline of 58 m. In the Bonn-Nörvenich region, RMS height differences of 11.6 and 2.7 m were calculated for baselines of 131 and 420 m respectively. Although these results were obtained using different scenes (and also time intervals between acquisitions), the approximately linear dependence of RMS height error vs.

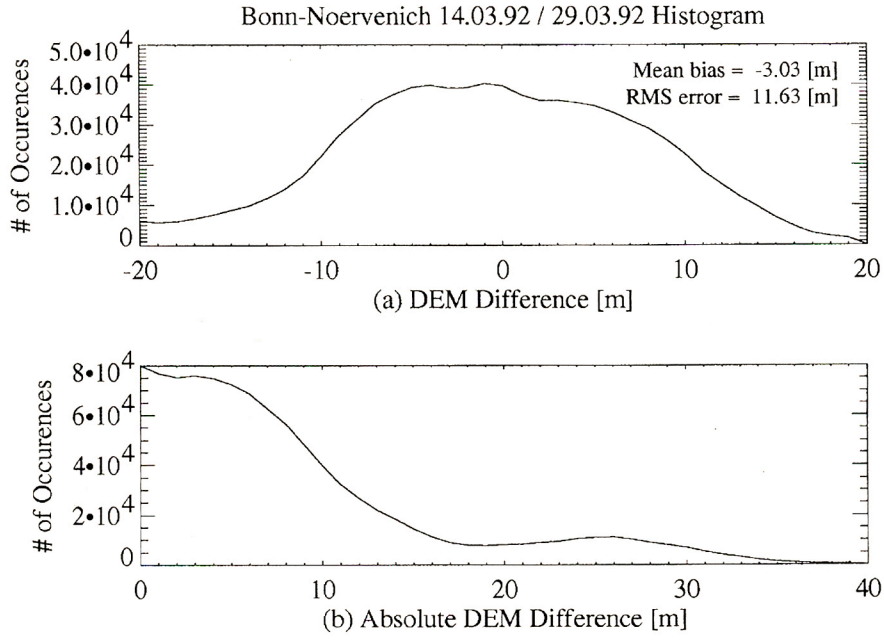

Figure 20 - Bonn-Nörvenich 14.03.92 / 29.03.92: (a) Histogram of height differences, (b) Histogram of absolute height differences.

baseline nevertheless indicates that the phase error term (Li and Goldstein, 1990) and propagation-change effects together dominate the RMS height error. The high accuracy achieved indicates that the geometry refinement described in Section 2.7 has mitigated the influence of the other error sources to a large extent.

5. CONCLUSIONS

We have provided an areal validation of height maps generated by repeat-pass satellite InSAR. RMS accuracies of 2.7 m were achieved over a 12 x 13 km area. Systematic biases in the height estimation were minimal over a 40 x 50 km standard ERS-1 quarter scene. Accuracy increases, as expected, with longer baselines, and decreases drastically in areas of low coherence (e.g. forest). Spectral-shift filtering dramatically decreases phase variance and is of critical importance for the large baselines that are optimal for the extraction of topography. Investigation of a coal-mining region demonstrated that ERS-1 InSAR-derived elevation models can improve upon even high quality DEMs.

The weakness of ERS-1 InSAR height derivation lies in hilly forested areas, where low coherences combine with topography to render height estimation problematic.

In order to further improve the achievable height accuracies, investigation is required to eliminate possible systematic biases, and better model phase unwrapping error sources, as well as atmospheric influences. Incorporation of a coarse elevation model during "flattening" and registration would also improve the achievable coherence.

6. ACKNOWLEDGEMENTS

This work was supported by an ESA contract within the GEOS Geocoding project (Schreier, 1993) at the D-PAF, Oberpfaffenhofen, Germany. Thanks are due to Steve Coulson, the ERS-1 FRINGE coordinator at ESA-ESRIN for providing the ERS-1 data, and to the Swiss Federal Office of Topography for providing the Swiss reference DEM. Erich Meier of RSL also contributed by preparing the Swiss reference DEM. Achim Roth, Michaela Matschke, and Walter Knöpfle of the D-PAF helped by providing the German reference DEM. Urs Wegmüller is thanked for the fruitful discussions on sources of (in)coherence. A thank you from DS also to Christoph Graf of RSL for assisting in 3D visualization of the DEM, and patiently answering map projection questions.

7. REFERENCES

Bamler R. & Just D., 1993. Phase Statistics and Decorrelation in SAR Interferograms. Proceedings of International Geoscience and Remote Sensing Symposium, Tokyo, Japan, 18-21 August 1993, 980-984

Curlander J.C., 1982. Location of Spaceborne SAR Imagery, IEEE Trans. on Geoscience and Remote Sensing, Volume GE-20, Number 3, July 1982, 359-364

Frei U., Graf K. Ch., & Meier E., 1993. Cartographic Reference Systems. In "SAR Geocoding: Data and Systems", Ed by G. Schreier (Karlsruhe: Herbert Wichmann Verlag GmbH), 213-234.

Gabriel A.K. & Goldstein R.M., 1988. Crossed Orbit Interferometry: Theory and Experimental Results from SIR-B, Intl. J. Remote Sensing, Volume 9, Number 5, 857-872.

Goldstein R.A., Zebker H.A. & Werner C.L., 1988. Satellite Radar Interferometry: Two-dimensional Phase Unwrapping, Radio Science, Volume 23, Number 4, 713-720.

Graf K.Ch., Suter M., Hagger J. & Nüesch D., 1994. Computer Graphics and Remote Sensing – A Synthesis for Environmental Planning and Civil Engineering, Proceedings of Eurographics'94, Oslo, Norway, 13 (3): 11-22, 519.

Haefner H., Holecz F., Meier E., Nüesch D. & Piesbergen J., 1993. Capabilities and Limitations of ERS-1 SAR Data for Snowcover Determination in Mountainous Regions, Proceedings of Second ERS-1 Symposium, Hamburg, Germany, 971-976.

Hartl P. & Thiel K.-H., 1993. Fields of Experiments in ERS-1 SAR Interferometry in Bonn and Naples, Proceedings of Symposium "From Optics to Radar: SPOT and ERS Applications", Cépaduès-Éditions, Paris, 525-534.

Holecz F., Meier E., Piesbergen J., Nüesch D. & Moreira J., 1994. Rigorous Derivation of Backscattering Coefficient, Proceedings of CEOS SAR Calibration Workshop, Ann Arbor, Michigan, 143-155.

Hutchins M., 1994. ERS-1 Off-Line Cal/Val Status Report, DRA/CIS(CSC2)/5/14-CR-001, Issue 1, Defence Research Agency, United Kingdom.

Li F.K. & Goldstein R.M., 1990. Studies of Multibaseline Spaceborne Interferometric Synthetic Aperture Radars, IEEE Trans. on Geoscience and Remote Sensing, Volume 28, Number 1, 88-97.

Lin Q., Vesecky J.F. & Zebker H.A., 1992. Registration of Interferometric SAR Images, Proceedings of International Geoscience and Remote Sensing Symposium, 26-29 May 1992, Houston, Texas, 1579-1581.

Lin Q., Vesecky J.F. & Zebker H.A., 1992. New Approaches in Interferometric SAR Data Processing, IEEE Trans. on Geoscience and Remote Sensing, Volume 30, Number 3, 560-567.

Madsen S.N., Zebker H.A. & Martin J., 1993. Topographic Mapping Using Radar Interferometry: Processing Techniques, IEEE Trans. on Geoscience and Remote Sensing, Volume 31, Number 1, 246-255.

Marquadt D.W., 1963. An Algorithm for Least Squares Estimation of Non-linear Parameters, Journal for the Society of Industrial and Applied Math, 11, 431-441.

Massonnet D., Feigl K., Rossi M. & Adragna F., 1994. Radar interferometric mapping of deformation in the year after the Landers earthquake, Nature, 369: 227-230.

Massonnet D., Rossi M., Carmona C., Adragna F., Peltzer G., Feigl K. & Rabaute T., 1993. The displacement field of the Landers earthquake mapped by radar interferometry, Nature, 364: 138-142.

Massonnet D., Perlant F. & Rabaute Th., 1993. Précision et Niveau d'artefacts dans les Calculs de Modèles Numériques de Terrain par Interférométrie, Proceedings of Symposium "From Optics to Radar: SPOT and ERS Applications", Cépaduès-Éditions, Paris, 511-523.

Meier E., Frei U. & Nüesch D., 1993. Precise Terrain Corrected Geocoded Images, In "SAR Geocoding: Data and Systems", Ed by G. Schreier (Karlsruhe: Herbert Wichmann Verlag GmbH), 173-185.

Meier E., 1989. Geometrische Korrektur von Bildern orbitgestützter SAR-Systeme, Remote Sensing Series, Volume 15, Department of Geography, University of Zürich, Zürich, Switzerland.

Prati C., Rocca F. & Guarnieri A.M., 1992. SAR Interferometry Experiments with ERS-1, Proceedings of First ERS-1 Symposium, Cannes, France, 211-218.

Rodríguez E. & Martin J.M., 1992. Theory and Design of Interferometric Synthetic Aperture Radars, IEE Proceedings-F, 139 (2): 147-159.

Roth A., Hügel T., Kosmann D., Matschke M. & Schreier G., 1993. Experiences with ERS-1 SAR Geopositional Accuracy, Proceedings of International Geoscience and Remote Sensing Symposium, Tokyo, Japan, 18-21 August 1993, 1450-1452.

Schreier G., Kosmann D. & Roth A., 1993. The D-PAF ERS-1 SAR Geocoding System GEOS, In "SAR Geocoding: Data and Systems", Ed by G. Schreier (Karlsruhe: Herbert Wichmann Verlag GmbH), 135-158.

Small D., Meier E.,Wegmüller U. & Nüesch D., 1994. Applications of Geocoded ERS-1 InSAR-derived Digital Terrain Information, Proceedings of CEOS SAR Calibration Workshop, Ann Arbor, Michigan, USA, 184-190.

Small D., Werner C. & Nüesch D., 1993b. Baseline Modelling for ERS-1 SAR Interferometry, Proceedings of International Geoscience and Remote Sensing Symposium, Tokyo, Japan, 18-21 August 1993, 1204-1206.

Small D., Werner C. & Nüesch D., 1993a. Registration of ERS-1 SLC Products for Interferometry, Proceedings of Fourth GEOSAR Workshop, Loipersdorf, Austria, 63-66.

Swiss Federal Office of Topography, 1993. Digital Height Model DHM25 Product Information, Wabern, Switzerland.

Wegmüller U. & Werner C., 1994. Analyses of Interferometric Land Surface Signatures, to appear in Proceedings of PIERS'94.

Wegmüller U., Werner C., Small D., Nïesch D. Analysis of Land Surface Signatures Using SAR Interferometry, RSL Report to ESA-ESTEC, Contact 134516, June 1994.

Werner C., Small D., Rosen P., Hensley S. & Zebker H.A., 1993. Techniques and Applications of SAR Interferometry for ERS-1, From Optics to Radar: SPOT and ERS Applications, Cépaduès-Éditions, Paris, 483-490.

Zebker H.A., Werner C., Rosen P. & Hensley S., 1994. Accuracy of Topographic Maps Derived from ERS-1 Interferometric Radar, IEEE Geoscience and Remote Sensing, 32 (4): 823-836.

Zebker H.A., Villasenor J. & Madsen S.N., 1992. Topographic Mapping from ERS-1 and SEASAT Radar Interferometry, Proceedings of International Geoscience and Remote Sensing Symposium, Houston, Texas, 26-29 May 1992, 387-388.